RSC Advances

PAPER

Cite this: *RSC Adv.*, 2015, **5**, 31064

# Porous graphene–carbon nanotube hybrid paper as a flexible nano-scaffold for polyaniline immobilization and application in all-solid-state supercapacitors†

Wei Fan, Yue-E Miao, Longsheng Zhang, Yunpeng Huang and Tianxi Liu*

Polyaniline (PANI) has been recognized as an ideal candidate for electrode materials in supercapacitors. However, the relatively low electrical conductivity and poor cyclic stability severely limit its potential applications. Therefore, a proper substrate with carefully designed nanostructures for PANI immobilization is highly desirable for realizing its full performance. In this study, three-dimensional porous graphene–carbon nanotube (p-GC) hybrid papers with high porosity, excellent electrical conductivity and good flexibility were utilized as a nano-scaffold for the *in situ* polymerization of PANI, thus obtaining flexible p-GC/PANI ternary hybrid papers with hierarchical nanostructures. The good electrical conductivity and optimized porous nanostructure of the p-GC hybrid paper provides improved conductive pathways and high surface area, ensuring the efficient utilization of the pseudocapacitance of PANI. Thus, the ternary hybrid paper exhibits a high specific capacitance of up to 409 F $g^{-1}$ at a current density of 10 A $g^{-1}$, as well as excellent rate and cyclic performance. Furthermore, the dimensional confinement of PANI particles within the p-GC framework effectively prohibits volume expansion and shrinkage upon electrolyte soakage and cycling. Therefore, the p-GC hybrid paper with tunable hierarchical nanostructures can act as a promising substrate to enhance the electrochemical properties of PANI or other electroactive materials and can be easily extended to the design of next-generation high-performance flexible supercapacitors.

Received 14th February 2015
Accepted 16th March 2015

DOI: 10.1039/c5ra02902c

www.rsc.org/advances

## 1. Introduction

Supercapacitors are electrochemical energy storage devices with unique properties such as high power density, long cyclic life, fast charge–discharge rates, and low maintenance cost.[1,2] Generally, there are two energy storage mechanisms for supercapacitors, namely, electrical double layer (EDL) capacitances and pseudocapacitances.[3] EDL capacitors, which can electrostatically store charges *via* reversible ion absorption at the electrode/electrolyte interface, commonly use carbon-based active materials with large surface area and good electrical conductivity.[4–6] Unfortunately, the relatively low capacitance prohibits the practical application of carbon-based materials. On the other hand, the pseudocapacitors, also called redox supercapacitors, undergo fast and reversible faradaic redox reaction at the surfaces of electroactive materials, thus achieving a considerably higher specific pseudocapacitance for faradaic electrodes over carbon-based materials using double-layer charge storage.[7,8] Polyaniline (PANI), known for the ease of synthesis, low cost, environmental friendliness and potentially large pseudocapacitance originating from its redox reactions, is one of the most promising electrode materials for pseudocapacitors.[9–12] However, PANI suffers from severe mechanical degradation problem caused by swelling and shrinkage during the doping and dedoping process, which greatly limits its application as an electrode material for supercapacitors. Therefore, to harvest the high capacitance of PANI while maintaining good cyclic stability, tremendous efforts have been made in the growth or polymerization of PANI on a variety of carbon nanomaterial templates, benefiting from the synergetic merits of both EDL capacitance and pseudocapacitance for high-performance supercapacitors.

To date, various carbon nanomaterials have been used as templates for the immobilization of PANI, including carbon nanotubes (CNTs),[13,14] mesoporous carbon,[15] hierarchically porous carbon monoliths,[16] carbon nanofibers[17] and graphene.[9–12,18–21] Surprisingly, the reported capacitance of PANI in these hybrid materials largely varies ranging from less than 500 F $g^{-1}$ to over 3400 F $g^{-1}$.[9,22] In fact, the mass specific capacitance of PANI in sulfuric acid has been theoretically estimated to be about 2000 F $g^{-1}$.[23] Nevertheless, it is practically

*State Key Laboratory of Molecular Engineering of Polymers, Department of Macromolecular Science, Fudan University, 220 Handan Road, Shanghai 200433, P. R. China. E-mail: txliu@fudan.edu.cn; Fax: +86-21-65640293; Tel: +86-21-55664197*

† Electronic supplementary information (ESI) available. See DOI: 10.1039/c5ra02902c

difficult to achieve such a high value due to the limited charge transfer rate, relatively low conductivity and unachievable full doping level. Such a significant variation of the reported capacitance of PANI may be caused by various factors, such as electrode components, device configuration and calculation method of capacitance.[22–24] Among them, one important factor is the difference of carbon substrate used for PANI immobilization. In particular, the structures of carbon substrate with different textural and porous properties have a great influence on the electrochemical performance of the resulting electrode materials.[25–30] For example, the capacitance of carbon/PANI hybrid electrode can reach 1270 F $g^{-1}$ by the deposition of PANI on hierarchically porous carbon monoliths,[16] while it only gives a low capacitance of 233 F $g^{-1}$ by growing PANI on graphene paper.[12] Furthermore, Wang *et al.* demonstrated that the porosity of the substrate is a key factor that can drastically affect the capacitance of PANI by preparing PANI@graphene hydrogel hybrid films with tunable pore sizes.[24]

In addition, among the various reports on carbon/PANI composites as supercapacitors, most of them are focused on powdery materials.[9,10,15,16,18] However, in most of the cases, conductive additives and polymer binders have to be used to stick the active materials onto metal foil when preparing working electrodes for electrochemical tests. The incorporation of insulating binders into the electrode not only makes the procedures more complex, but also impairs the electrical conductivity and wastes energy on unwanted inner resistance. Thus, it is preferable to directly fabricate free-standing carbon/PANI composites with high electrical conductivity for capacitance testing. To date, free-standing carbon substrates, such as vacuum-filtration graphene films,[31–35] graphene foams,[36–38] hydrogels,[24,39,40] CNT sponges[41] and carbon fabrics,[42,43] have been reported for the immobilization of PANI, making them promising candidates for application in flexible supercapacitors. However, previous reports scarcely reveal careful control over the morphology of carbon substrate and reasonable order of individual active material in the composites. Therefore, a proper substrate with high porosity, excellent electrical conductivity and good flexibility for PANI immobilization is highly desirable for the efficient utilization of pseudocapacitance originating from PANI, thus leading to an enhanced supercapacitor performance.

In the present work, three-dimensional (3D) porous graphene–carbon nanotube (p-GC) hybrid papers, recently developed by our group,[44] are applied to provide a conductive and flexible network for PANI immobilization. As previously demonstrated, free-standing p-GC papers with uniform and controllable porous structures can be fabricated by a template directed method. The face-to-face restacking of graphene sheets in the p-GC papers can be completely prevented by polystyrene (PS) nanospheres and CNT spacers, resulting in highly porous 3D networks. In addition, CNTs acting as both spacers and conductive linkers between graphene layers contribute to the much higher porosity and improved electrical conductivities as compared with bare graphene paper. The unique structure of p-GC papers thus can offer a number of distinct advantages for the immobilization of PANI as follows: (1) given that the p-GC paper is highly porous, it is highly accessible to ions and molecules, ensuring the uniform deposition of PANI by the *in situ* polymerization of aniline; (2) the content of PANI can be simply controlled by the initial aniline concentration with the weight fraction of PANI in ternary p-GC/PANI hybrid papers being easily regulated (*e.g.* from 19 wt% to 51 wt% in our case); (3) the porosity of graphene–CNT papers can be easily tuned by changing the initial loading level of PS nanospheres, allowing us to readily explore its effect on the capacitance of PANI; (4) dimensional confinement of PANI within p-GC framework effectively prohibits volume expansion and shrinkage upon electrolyte soakage and cycling, leading to improved electrochemical stability; and (5) the free-standing p-GC papers are highly electrically conductive and mechanically strong, which enables their direct use as flexible binder-free electrodes for supercapacitors. Therefore, the unique nanostructure of p-GC papers makes them promising substrates for PANI immobilization with an efficient utilization of pseudocapacitance. The resulting ternary p-GC/PANI hybrid papers show promising applications in flexible supercapacitors.

## 2. Experimental section

### 2.1. Materials

Natural graphite powder (325 meshes) was purchased from Alfa-Aesar. Multiwalled carbon nanotubes (length, 10–30 μm; outer diameter, 40–50 nm; purity, 95%), produced by chemical vapor deposition method, were supplied by Chengdu Institute of Organic Chemistry, Chinese Academy of Sciences, China. Aniline and styrene were purchased from Sigma-Aldrich. Potassium persulfate (KPS), ammonium persulfate (APS), ethanol, 98% $H_2SO_4$, 30% $H_2O_2$, $KMnO_4$, $NaNO_3$ and 37% HCl were supplied by China Medicine Co. Aniline and styrene were purified by distillation, and other reagents were used as received without further treatment. Deionized (DI) water was used throughout all the experiments.

### 2.2. Preparation of PS and aqueous suspension of GO–CNT hybrid

Monodispersed PS spheres with diameters of ~400 nm were synthesized according to the procedures reported elsewhere.[45] After centrifugation and washing processes, the PS nanospheres were dispersed in DI water for further use. A stable aqueous solution of graphene oxide (GO)–CNT hybrid was prepared using a method previously reported by us.[33,46] Briefly, graphene oxide was synthesized by Hummers method,[47] and exfoliated to give a brown dispersion (1.0 mg $mL^{-1}$) of GO under ultrasonication. The aqueous colloidal suspensions of GO sheets were then mixed with CNT conglomerations with a weight ratio of 1 : 1, followed by ultrasonication for 1 h. This suspension was centrifuged for 30 min at 8000 rpm to remove the unstabilized CNTs, thus giving a stable suspension of GO–CNT hybrids.

### 2.3. Fabrication of porous graphene–CNT hybrid paper

A small amount of PS suspension (0.5 mg $mL^{-1}$) was added to 60 mL of 0.5 mg $mL^{-1}$ GO–CNT suspension drop by drop, and

the resulting mixture was sonicated for another 2 h. Subsequently, the mixed suspension containing PS spheres and GO–CNT hybrids was vacuum-filtered through a poly(vinylidene fluoride) (PVDF) membrane filter (220 nm pore size, Durapore® from Sigma-Aldrich). To obtain a free-standing hybrid paper, the paper was dried at room temperature, and then carefully peeled off from the membrane filter. Subsequently, the as-prepared GO–CNT/PS hybrid paper was placed in an alumina crucible and calcinated in a horizontal furnace under pure nitrogen gas atmosphere at 800 °C with a heating rate of 5 °C $min^{-1}$, and allowed to stand for 4 h at the final temperature. Thus, 3D porous graphene–CNT (p-GC) hybrid papers were obtained. The thickness of the p-GC hybrid papers was varied by changing the amount of the mixed suspension for vacuum filtration. p-GC paper with a thickness of ~11 μm was obtained from 30 mg GO–CNT hybrid, while p-GC paper with a thickness of ~19 μm was obtained from 60 mg GO–CNT hybrid. Moreover, the weight ratio of PS to GO–CNT was 6 : 1 for both the samples. The porosity of the graphene–CNT hybrid papers was also tuned by changing the initial loading amount of PS nanospheres. The p-GC paper was obtained from the mixed suspension containing PS spheres and GO–CNT hybrids with weight ratio of 6 : 1, and porous graphene–CNT hybrid paper with half the amount of PS nanospheres was denoted as p-0.5-GC. For comparison, porous graphene paper and neat graphene–CNT (GC) hybrid paper were also fabricated in a similar way without adding CNTs or PS.

### 2.4. Immobilization of PANI particles on p-GC hybrid paper

Hierarchical p-GC/PANI ternary hybrid papers were synthesized by the *in situ* polymerization of aniline monomer in the presence of p-GC hybrid paper. Typically, a small amount of aniline and APS (molar ratio: 4/1) was added into 1 M $H_2SO_4$ solution. Then, the p-GC hybrid paper was immersed into the above-mentioned solution, and allowed to react at 0 °C for 6 h without stirring. The as-obtained p-GC/PANI ternary hybrid papers were then washed with water, and dried at room temperature. With increasing aniline concentrations to 0.01 M, 0.03 M and 0.05 M, the corresponding p-GC/PANI ternary hybrid papers were obtained and labelled as p-GC/PANI1, p-GC/PANI3 and p-GC/PANI5, respectively. For comparison, PANI particles were immobilized on GC and p-0.5-GC papers using the same method. Moreover, PANI powder, without any template, was also polymerized *in situ* under the same conditions.

### 2.5. Characterization

Morphologies of the samples were investigated using field emission scanning electron microscopy (FESEM, Zeiss) at an acceleration voltage of 5 kV. Transmission electron microscopy (TEM) observation was performed with a JEOL 2100 TEM under an accelerating voltage of 200 kV. The Brunauer–Emmett–Teller (BET) surface area was measured using a Belsorp-max surface area detecting instrument by nitrogen physisorption at 77 K. Raman spectra were obtained on a LabRam-1B French Dilor Com ($\lambda_{ex}$ = 632.8 nm). X-ray diffraction (XRD) patterns of the samples were obtained on an X'Pert Pro X-ray diffractometer with Cu $K_\alpha$ radiation ($\lambda$ = 0.1542 nm) under a voltage of 40 kV and a current of 40 mA. Thermogravimetric analysis (Pyris 1 TGA) was performed under nitrogen flow from 100 to 800 °C at a heating rate of 10 °C $min^{-1}$.

### 2.6. Electrochemical measurements

All the electrochemical experiments were carried out on a CHI 660C electrochemical workstation at room temperature. In a two-electrode system, p-GC/PANI ternary hybrid papers were used as working electrodes, whereas a stainless steel foil was used as the current collectors and poly(vinyl alcohol) (PVA)/$H_2SO_4$ gel was used as the separator, thus forming highly flexible and foldable all-solid-state supercapacitors. The as-prepared hybrid papers were cut into 10 × 10 $mm^2$ squares and used directly as the binder-free electrode material with the mass loading of about 1.2 mg for a single electrode. The gel electrolyte was fabricated by mixing 6 g $H_2SO_4$ and 6 g PVA in 60 mL deionized water and heating up to 90 °C for 2 h with vigorous stirring. Two slices of p-GC/PANI ternary hybrid papers were immersed in a clear solution of PVA/$H_2SO_4$ gel electrolyte for 10 min. The resulting electrolyte-filled electrodes were solidified for 8 h at room temperature. Finally, the two as-obtained electrodes were symmetrically integrated together to obtain all-solid-state supercapacitors. Both cyclic voltammetry (CV) curves collected at different scan rates and galvanostatic charge–discharge curves were measured in voltages ranging from −0.2 to 0.8 V. Electrochemical impedance spectroscopy (EIS) was recorded in the frequency range from $10^5$ to 0.01 Hz at the open circuit potential with an AC voltage amplitude of 5 mV.

The specific capacitance $C_s$ (F $g^{-1}$) of the samples was estimated from the discharge process according to the following equation:

$$C_s = \frac{4I\Delta t}{\Delta V \times m} \quad (1)$$

where $I$ is the current loaded (A), $\Delta t$ is the discharge time (s), $\Delta V$ is the potential change during discharge process, and $m$ is the total mass of the two electrodes (g).

## 3. Results and discussion

Due to the hydrophilic oxygen groups attached to the GO basal planes and edges, GO can easily form a dark brown aqueous colloidal suspension under sonication. From the AFM image and the corresponding height profile shown in Fig. S1,† it can be seen that the thickness of GO sheets ranges from 0.9 to 1.1 nm, indicating that large amounts of oxygen-containing groups are introduced onto GO sheets during the Hummers oxidation process. On the other hand, owing to strong van der Waals interactions and high conformational rigidity, the pristine CNTs show very limited dispersibility in aqueous solutions. In our previously reported strategy, GO sheets were utilized as effective dispersants to stabilize pristine CNTs in aqueous media.[33,46] It was found that a series of stable black dispersions can be obtained with the weight ratio of GO to CNTs larger than 1/2, indicating a strong stabilizing ability of the GO sheets for

 

pristine CNTs in water. Based on our previous reports,[44] an optimized weight ratio of 1/1 for better electrical performance was selected and used throughout all the experiments in this study. It is reasonable to suppose that the π-conjugated multiple aromatic regions of GO sheets could interact with the sidewalls of CNTs through the π–π stacking interaction, while the hydrophilic oxygen groups maintain the good water dispersibility of the GO–CNT complexes. TEM observations (Fig. 1) strongly confirm the formation of GO–CNT hybrids. As shown in Fig. 1a and b, hair-like CNTs were randomly adsorbed on the smooth surface of GO sheets, without individual GO sheets or CNTs in the view. This phenomenon clearly indicates strong interactions between these two types of nanoelements during the formation of GO–CNT hybrids. The inset in Fig. 1a shows the aqueous dispersion of GO–CNT hybrids with weight ratios of 1/1 after allowing it to settle for one month, indicating the good dispersibility of the hybrid. Fig. 1c and d shows TEM images of PS spheres, displaying good uniformity in size with an average diameter of ~400 nm.

Graphene-based paper-like bulk materials with lightweight property, robust mechanical properties and feasibility can be easily fabricated through vacuum-assisted self-assembly, which is of great significance for practical applications.[48,49] Herein, the stable dispersion of GO–CNT hybrids in water is beneficial for the subsequent filtration process, resulting in the formation of free-standing hybrid papers with CNTs imbedded uniformly in GO frameworks. Moreover, by incorporating PS nanospheres into the GO–CNT hybrid dispersion, 3D porous graphene–CNT hybrid papers can be prepared by the vacuum filtration of the mixture suspension, followed by calcination to remove the PS nanospheres to generate 3D nanopores, as well as reduce GO into graphene, simultaneously (Scheme 1). This template directed method can form much more uniform and controllable porous structures, which can boost ion and electron movement in electrochemical processes.[28] By changing the initial loading amount of PS nanospheres, the porosity of graphene–CNT hybrid papers can be easily tuned because PS nanospheres act as the pore-forming template. Here, porous graphene–CNT hybrid papers obtained from PS and GO–CNT with weight ratios of 1 : 6 and 1 : 12 were prepared and denoted as p-GC and p-0.5-GC, respectively. The SEM images of both the surface and cross-section of pure GC, p-0.5-GC and p-GC hybrid papers are shown in Fig. 2. All the hybrid papers clearly exhibit a well-packed layered structure through the entire cross-sections, indicating that graphene–CNT hybrids can be assembled to form parallel arranged nanostructures under filtration-induced directional flow. For a pure GC hybrid paper (Fig. 2a and b), CNTs are incorporated between large lateral dimensional graphene layers, resulting in the formation of sandwiched structures. Unlike pure GC, evenly distributed uniform pores can be observed between the parallel arranged graphene–CNT frameworks (Fig. 2c–f), resulting from the removal of PS templates, which leaves behind an open porous structure. The porous structure thus successfully obtained duplicates of the original template structure without any collapse because of the interconnected nature of the multilayered graphene walls in the assembled 3D structure. The mechanical strength of graphene, pore size, and thermal stability synergistically help to preserve the porous structure even after calcination. By comparing p-0.5-GC (Fig. 2c and d) with p-GC (Fig. 2e and f), the roughness and porosity of the paper increase obviously with the increase of PS content, indicating that PS nanospheres act as the pore-forming template. However, further increasing the amount of PS nanospheres will result in the fracture of the paper. In addition, a digital image inserted in Fig. 2f illustrates the high flexibility of the p-GC hybrid paper. Furthermore, it is noteworthy that without CNTs, the porous graphene paper has a much more compact layered structure, as shown in Fig. S2.† Here, CNTs act as both the spacers and conductive linkers between individual graphene sheets, which can destroy the well-ordered structure of layered graphene, thus contributing to the higher porosity and conductivity.[50]

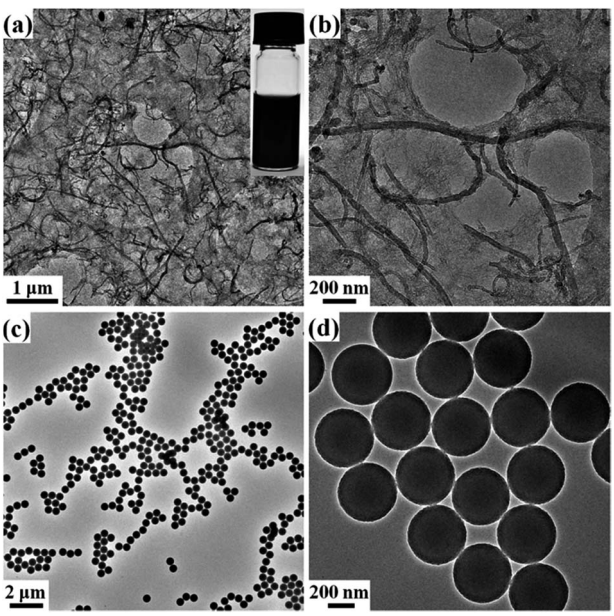


Fig. 1 (a and b) TEM images of GO–CNT hybrids with weight ratio of 1 : 1, and (c and d) PS nanospheres at low (left) and high (right) magnifications, respectively. Inset in (a) shows the digital image of GO–CNT hybrid aqueous suspension after allowing it to settle for one month.

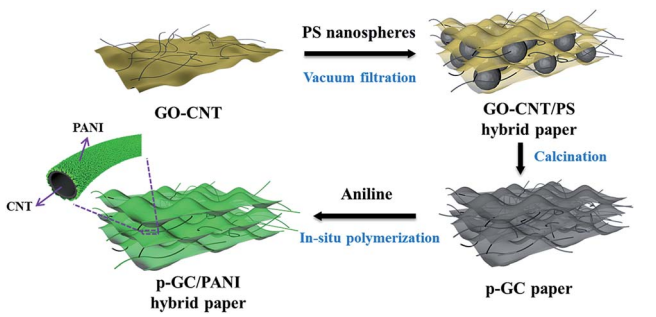


Scheme 1 Schematic illustration for the preparation of porous graphene–CNT/PANI hybrid paper.

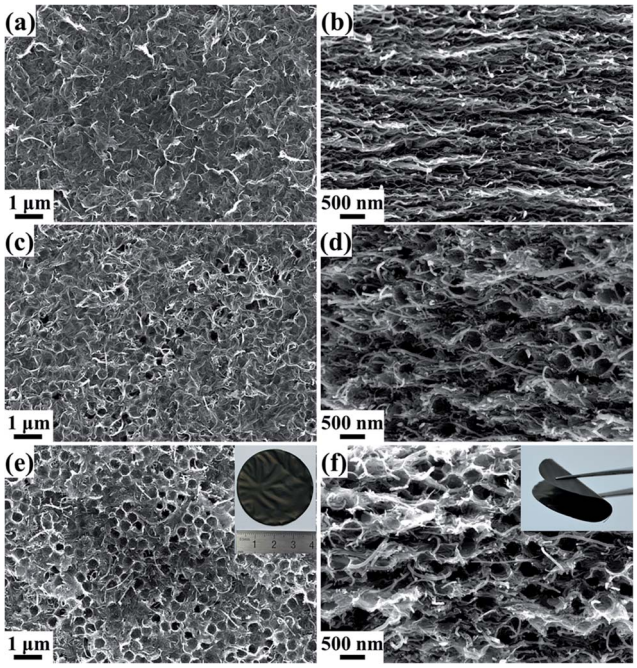


Fig. 2 FESEM images of (a and b) GC, (c and d) p-0.5-GC, (e and f) p-GC. The left column shows the surface and the right column shows the cross-section of the papers. Insets in (e) and (f) show the digital images of the free-standing p-GC paper peeled off from filter membrane and held by a tweezer, showing a good flexibility.

The amount of PS nanospheres has a great influence on the BET specific surface area of the resulting porous hybrid paper, which is investigated by nitrogen isothermal adsorption. Fig. 3 shows the nitrogen physisorption isotherms of GC, p-0.5-GC and p-GC. The isotherm curves show a type IV isotherm with a steep increase of nitrogen absorption at a high relative pressure ($P/P_0 = 0.80$–$0.99$), indicating that the main pore volume is contributed by the large-sized pores. The surface area of GC, p-0.5-GC and p-GC are 121, 350 and 556 $m^2\ g^{-1}$, respectively, suggesting that the introduction of PS nanospheres between 2D graphene sheets efficiently limits the face-to-face stacking between graphene layers. Furthermore, p-GC paper has a much larger surface area over porous graphene paper without CNTs (247 $m^2\ g^{-1}$, Fig. S3†), which is possibly due to the existence of

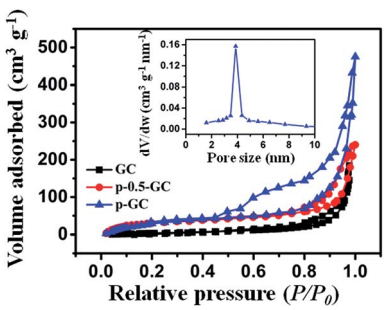


Fig. 3 Nitrogen sorption isotherms of GC, p-0.5-GC and p-GC. The inset shows the corresponding pore size distribution of p-GC hybrid paper.

CNTs in this 3D hierarchical structure acting as spacers between individual graphene layers. The inset in Fig. 3 shows the pore size distribution of the p-GC sample obtained by the Barrett–Joyner–Halenda (BJH) method. Narrowly distributed pore size at mesoporous range of about 4 nm further indicates that mesopores could be generated by CNT spacers. Therefore, the largely improved surface area of p-GC hybrid paper can be attributed to the co-existence of CNTs as spacers and PS nanospheres directed nanopores, which can completely prevent graphene sheets from restacking.

The resulting p-GC hybrid paper with tunable porous structure, high electrical conductivity and flexibility, is a good template for the further growth of PANI. The FESEM images of both the surface and cross-section of p-GC/PANI ternary hybrid papers with different PANI loadings are respectively shown in Fig. S4† and 4. As shown in Fig. S4,† it is possible to achieve homogeneously distributed PANI particles adhered to the surface of p-GC hybrid paper substrates *via in situ* polymerization. It can be observed that nano-sized PANI particles can not only grow on the surface (Fig. S4†), but also inside (Fig. 4) the pores of p-GC papers with a uniform distribution. The inset in Fig. 4b illustrates the high flexibility of p-GC/PANI3 ternary hybrid paper, which can be bent and held by a tweezer. The content and morphology of the PANI grown on the p-GC paper can be easily controlled by varying the initial aniline concentrations. At a low aniline concentration, the layered and porous structure of the p-GC paper does not change considerably and only a thin layer of PANI can be observed, as shown in Fig. 4a and d. Homogeneously distributed but thicker layers of PANI on both graphene sheets and CNTs can be achieved at a higher concentration of aniline (0.03 M), as indicated by the growing diameter of CNTs (Fig. 4b and e). Graphene sheets and CNTs within the hybrid paper serve as heterogeneous nucleation sites for the polymerization of PANI in solution because aromatic molecules can strongly interact with the basal plane of graphitic surfaces through π–π interaction. Moreover, the porous structures can be still maintained in this condition as indicated by red arrows in Fig. 4a and b, which could provide an extremely large specific surface area of electrodes and facilitate the full use of the large pseudocapacitance of PANI. However, a further increase in the aniline concentration leads to a more obvious urchin-like morphology of PANI (Fig. 4c and f), which may be due to the rapid polymerization rate of aniline at high concentrations. In addition, the porous structure originating from PS removal can hardly be observed from the p-GC/PANI5 hybrid paper because the excess loading of PANI may block these pores, and thus lead to a suppressed surface area. The loading amounts of PANI are calculated from the TGA curves (Fig. S5†) to be 19 wt%, 32 wt%, and 51 wt% for p-GC/PANI1, p-GC/PANI3, and p-GC/PANI5, respectively.

To further confirm the successful immobilization of PANI on the p-GC paper, the XRD and Raman spectra of GO–CNT, p-GC, PANI and p-GC/PANI3 are collected and shown in Fig. 5. As shown in Fig. 5a, the XRD pattern of the GO–CNT hybrid shows two obvious diffraction peaks at $2\theta = 10.6°$ and 26.4°, indicating the co-existence of GO and CNTs. The peak at $2\theta = 10.6°$ disappears for p-GC, suggesting the successful

 

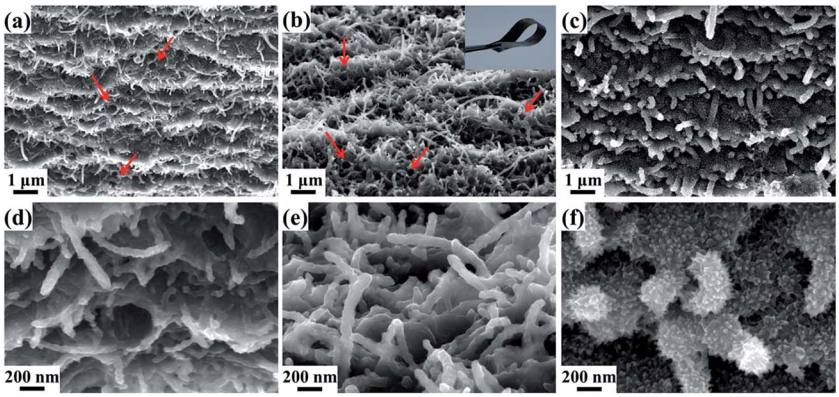


Fig. 4 Cross-sectional FESEM images of (a and d) p-GC/PANI1, (b and e) p-GC/PANI3, and (c and f) p-GC/PANI5 papers at (a–c) low and (b–f) high magnifications.

reduction of GO to form graphene during the calcination process. For neat PANI, the reflection peaks appear at $2\theta$ = 19.7° and 25.3°, respectively, corresponding to the (020) and (200) crystal planes of PANI in its emeraldine salt form.[9,10] The p-GC/PANI3 hybrid paper shows an obvious peak at $2\theta = 26.4°$ with a broad peak from $2\theta$ = 10° to 30°, indicating the successful immobilization of PANI on p-GC paper. Fig. 5b shows the Raman spectra of p-GC, PANI and p-GC/PANI3. For carbon materials like p-GC, there are always two peaks appearing at 1300–1400 $cm^{-1}$ and 1500–1600 $cm^{-1}$, which are denoted as the D band and G band, respectively. The p-GC/PANI3 hybrid paper shows three apparently new emerging peaks at approximately 1163, 1250, and 1478 $cm^{-1}$, which can be ascribed to C–H bending in the benzene- or quinine-type rings, in-plane ring deformation, and C=N stretching in emeraldine base (imines) of PANI, respectively.[10,51] These results clearly confirm that PANI has been successfully decorated onto the p-GC paper substrates.

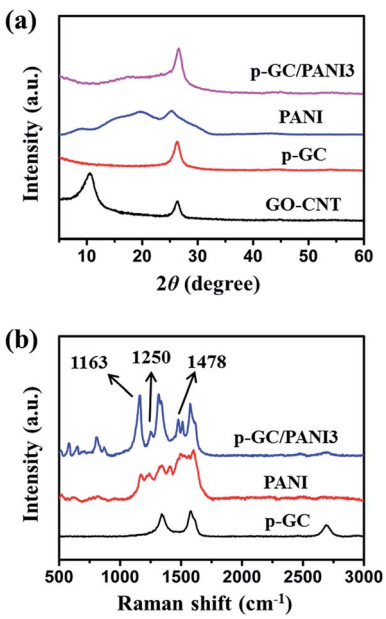


Fig. 5 (a) XRD patterns of GO–CNT, p-GC, PANI and p-GC/PANI3, and (b) Raman spectra of p-GC, PANI and p-GC/PANI3.

The capacitive performance of p-GC/PANI ternary hybrid papers was evaluated *via* a two-electrode system with a polymer gel electrolyte. Fig. 6a and b illustrate the cyclic voltammetry (CV) and galvanostatic charge–discharge curves of GC, p-GC, p-GC/PANI1, p-GC/PANI3 and p-GC/PANI5 papers, respectively. The CV curves of both GC and p-GC exhibit an approximately rectangular shape, while the charge–discharge curves display a triangular shape, indicating a typical EDL capacitance of carbon materials. The capacitance of p-GC paper is slightly larger than that of GC paper, which can be attributed to the enhanced surface area of the 3D porous nanostructure. Besides, the thickness of p-GC paper is optimized in this study to achieve a better electrochemical performance. As shown by the CV curves in Fig. S6,† the p-GC paper with thickness of about 11 μm has a larger specific capacitance than that of about 19 μm. This can be explained by the fact that thicker film would increase the diffusion lengths and transport resistance of electrolyte ions in the electrode. However, further reducing the film thickness will cause the fracture of the film. Therefore, the p-GC paper with an optimized thickness and electrochemical performance was chosen for PANI immobilization in this work. According to the literature,[52] an aromatic molecule can strongly interact with the basal plane of graphitic surfaces through π–π interaction, thus ensuring good electron transfer between the conjugated structure of PANI and the basal plane of graphene sheets or the sidewall of CNTs. This is perfectly confirmed by CV curves, in which two pairs of redox peaks are clearly shown (Fig. 6a), and the galvanostatic charge–discharge curves, in which a plateau appears in the voltage range from 0.2 to 0.4 V (Fig. 6b), for the p-GC/PANI ternary hybrid papers. The redox peaks in the CV curves and the plateau in the charge–discharge curves also indicate that p-GC/PANI hybrid papers can provide both faradic capacitance and EDL capacitance. Moreover, the peak currents of all p-GC/PANI ternary hybrid papers are higher than those of p-GC paper, indicating an obvious improvement in capacitance after its combination with pseudocapacitance materials.

Specific capacitances (against the total weight of a single electrode material) estimated from the discharge process at a

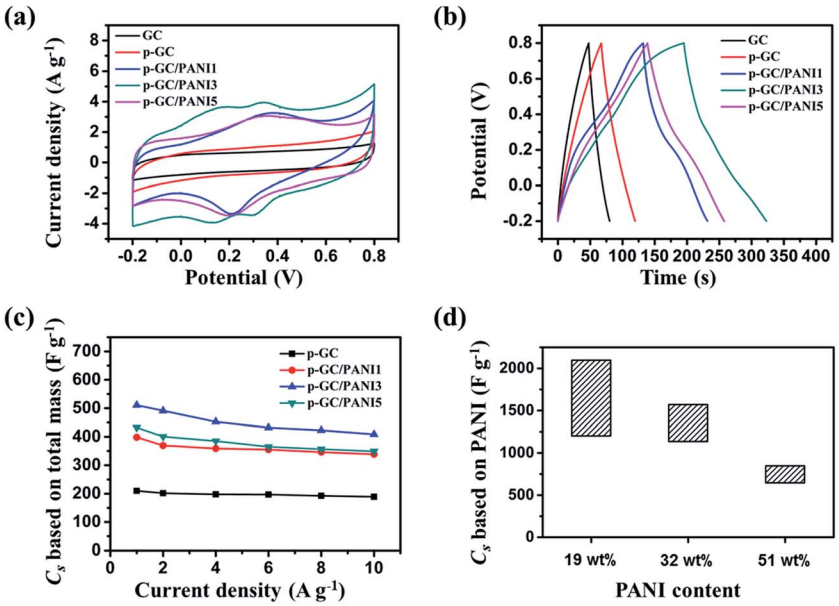


Fig. 6 (a) CV curves of GC, p-GC, p-GC/PANI1, p-GC/PANI3 and p-GC/PANI5 papers at a scan rate of 10 mV $s^{-1}$. (b) Galvanostatic charge–discharge curves of GC, p-GC, p-GC/PANI1, p-GC/PANI3 and p-GC/PANI5 papers within a potential window of −0.2–0.8 V at a current density of 1 A $g^{-1}$. (c) Specific capacitance ($C_s$) of p-GC/PANI hybrid papers against the total weight of PANI and p-GC, and (d) $C_s$ of PANI against its own weight at a current density of 1 A $g^{-1}$.

current density of 1 A $g^{-1}$ for GC, p-GC, p-GC/PANI1, p-GC/PANI3 and p-GC/PANI5 papers were 129, 209, 398, 511, and 432 F $g^{-1}$, respectively. The improved capacitance of p-GC/PANI3 hybrid paper can be attributed to the unique porous nanostructure, which maximizes the exposure of their surfaces to electrolytes, and the effective PANI immobilization further enhances the capacitance by introducing a pseudocapacitance. In addition, our previous study[44] indicated that CNTs inserted between graphene layers can act as effective spacers and conductive linkers, which can also contribute to a higher specific capacitance. The specific capacitances of the prepared electrode materials as a function of current densities are shown in Fig. 6c. Obviously, the p-GC/PANI3 hybrid paper has the highest specific capacitance among all the samples in a wide range of current densities. Even at the high current density of 10 A $g^{-1}$, almost all of the p-GC/PANI hybrid papers maintain a high retention efficiency of more than 80% (409 F $g^{-1}$ for p-GC/PANI3), indicating the remarkably improved rate performance with better sustainability to high currents. Besides, the p-GC/PANI3 hybrid paper exhibits an excellent electrochemical behavior over a wide range of scan rates (Fig. S7†), further indicating the good rate ability of the as-synthesized electrode materials.

The specific capacitance of PANI against its own weight (Fig. 6d) is also calculated using the method reported by Wang and co-workers.[24] Given that graphene–CNT in the hybrid paper could potentially contribute to EDL capacitance, the exact mass specific capacitance range of PANI was estimated by subtracting the contribution of graphene–CNT from the specific capacitance of p-GC/PANI hybrid papers. Taking the p-GC/PANI3 hybrid paper (PANI content of 32 wt%) as an example, the specific capacitance against the total weight of PANI and p-GC is 511 F $g^{-1}$ at a current density of 1 A $g^{-1}$, and that of PANI is found to fall in between 1136 F $g^{-1}$ and 1572 F $g^{-1}$ (Fig. 6d). The value of 1136 F $g^{-1}$ is obtained by assuming that p-GC provides its full capacitance (209 F $g^{-1}$), while the contribution of p-GC to the capacitance is totally neglected for the value of 1572 F $g^{-1}$. The content of PANI in the p-GC/PANI hybrid papers has a significant impact on its specific capacitance. As shown in Fig. 6d, the specific capacitance of PANI against its own weight decreases with increasing content of PANI in the hybrid papers. When the capacitance contribution of graphene–CNT is excluded, the resulting specific capacitance of PANI varies from 2097 F $g^{-1}$ (for p-GC/PANI1 containing 19 wt% PANI) to 848 F $g^{-1}$ (in the case of p-GC/PANI5 with 51 wt% PANI). It has been suggested that the faradaic reaction mainly occurs at the interface between PANI and the electrolyte.[23] Increasing the coating thickness of PANI makes the charge transfer rather difficult across PANI, thus severely limiting the capacitance contribution of the interior part of PANI, and leading to the reduction of the overall specific capacitance of PANI. Furthermore, a thinner PANI coating gives rise to higher specific surface area, also resulting in a higher EDL capacitance.

The porous structure is found to be another key factor that can drastically influence the capacitance of PANI. As demonstrated in Fig. 3, the porosity of graphene–CNT papers can be easily tuned by changing the initial loading amount of PS nanospheres. Here, the graphene–CNT/PANI hybrid paper containing 32 wt% of PANI was taken as an example to study the effect of porosity on the capacitance of PANI. As indicated in Fig. S8,† the specific capacitances of the graphene–CNT/PANI hybrid papers decrease dramatically with lower porosity, *i.e.*, less PS nanospheres added. Specific capacitances (against the total weight of PANI and p-GC in a single electrode) estimated

 

from the discharge process at a current density of 1 A $g^{-1}$ for GC/PANI3, p-0.5-GC/PANI3 and p-GC/PANI3 papers were 316, 432 and 511 F $g^{-1}$, respectively. This can be explained by the greatly enhanced specific surface areas with the increase of porosity, which can provide short pathways for both mass and charge transport and decreased diffusion resistance of electrolyte ions in the electrode. In addition, the specific capacitance of PANI against its own weight is also affected significantly by the porous structure of the graphene–CNT paper substrate. The higher porosity leads to higher specific capacitance, indicating that porous structures more efficiently utilize the pseudocapacitances provided from PANI. For p-GC/PANI3 paper, the specific capacitance of PANI against its own weight is estimated to be between 1136 F $g^{-1}$ and 1572 F $g^{-1}$ at a current density of 1 A $g^{-1}$ (Fig. S8b†). However, the GC paper prepared without PS spheres has only limited porosity, leading to an increased resistance for ion transport within the GC/PANI3 hybrid paper. Consequently, the specific capacitance of PANI against its own weight decreases to a range from 543 F $g^{-1}$ to 987 F $g^{-1}$ (Fig. S8b†). The deposition of PANI in GC paper further blocks these pores and makes the diffusion of electrolyte ions difficult, leading to worse electrochemical performance of PANI. Therefore, the porous graphene–CNT paper with high porosity and large surface area is an excellent candidate for the immobilization of PANI or other pseudocapacitive materials.

Further understanding of the ion diffusion in porous hybrid papers was obtained by conducting impedance measurements in the frequency range of 100 kHz to 0.01 Hz. Nyquist plots of p-GC, PANI, and p-GC/PANI3 papers are displayed in Fig. 7a. The Nyquist plot of p-GC/PANI3 hybrid paper shows a straighter line in the low-frequency region and a smaller semi-circle in the high frequency region as compared to pure PANI. This indicates that the capability of fast ion diffusion is maintained even after PANI is deposited within the p-GC paper. The cycle life tests of p-GC/PANI3 hybrid paper were conducted by galvanostatic charge–discharge measurements at a current density of 1 A $g^{-1}$. As shown in Fig. 7b, the p-GC/PANI3 hybrid paper electrode keeps a high retention ratio of 85% after 1000 cycles, illustrating the good stability of the all-solid-state supercapacitors. This is in sharp contrast to previous reports, which state that conventional PANI-based supercapacitors are susceptible to mechanical degradation as a result of swelling and shrinkage caused by doping and dedoping. The improved electrochemical stability of the p-GC/PANI3 hybrid paper can be explained as follows. First, the dimensional confinement of PANI within p-GC framework can effectively prevent it from severely swelling and shrinking during cycling. Besides, the strong adhesion of PANI on p-GC through π–π interaction can also maintain the stability. Furthermore, the electrochemical performance of p-GC/PANI3 hybrid paper was measured under different bending angles to demonstrate the flexibility and foldability of the symmetric electrochemical capacitor device. As shown in Fig. 7c, no significant difference can be observed between the CV curves under various deformations, further demonstrating the good stability, high flexibility and foldability of the symmetric electrochemical capacitor device based on p-GC/PANI hybrid papers.

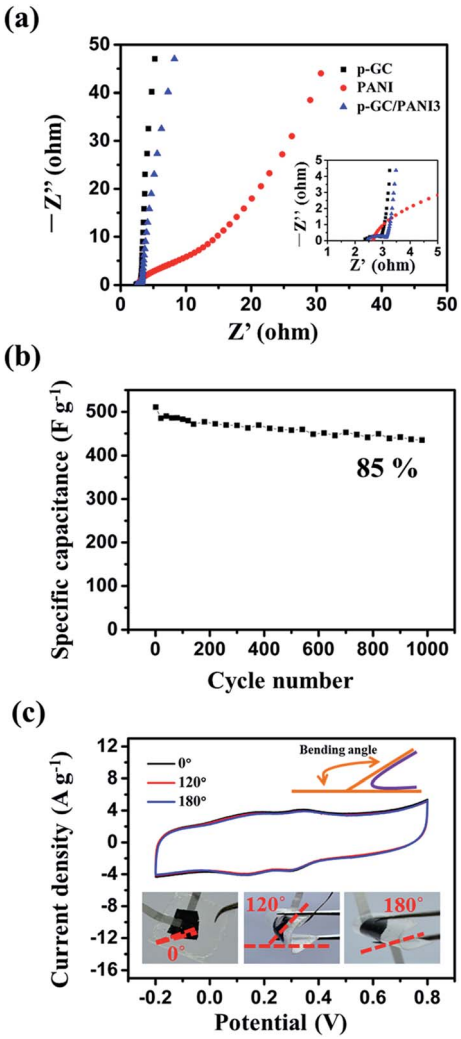


Fig. 7 (a) Nyquist plots for p-GC, PANI and p-GC/PANI3 papers. $Z'$: real impedance. $Z''$: imaginary impedance. Inset shows an enlarged scale. (b) Cycling stability of p-GC/PANI3 paper upon charging–discharging at a current density of 1 A $g^{-1}$. (c) CV curves obtained at different bending angles of the flexible supercapacitor based on p-GC/PANI3 ternary hybrid paper. Digital images in the inset display the direct view of supercapacitor device bending at different angles.

## 4. Conclusions

In conclusion, 3D porous graphene–carbon nanotube hybrid papers were obtained as a conductive, flexible and free-standing nano-scaffold for PANI immobilization. The p-GC papers inherit uniform and controllable porous structures, improved electrical conductivities and mechanical stability with CNTs acting as both spacers and conductive linkers between individual graphene sheets, thus providing a number of distinct advantages for the immobilization of PANI. The resulting p-GC/PANI ternary hybrid paper based binder-free supercapacitor device enabled the combination of high capacitance, high rate capability, and long cycling life, based on the synergistic function of 3D porous nanostructure, effective CNT intercalation and PANI immobilization. In addition, it has been

demonstrated that loading amount and porous structure have great influences on the capacitance of PANI, indicating that the proper nano-engineering of the electrode structure is the key to realize its full performance. Therefore, this work highlights the great potential of using 3D porous graphene–carbon nanotube hybrid papers as unique frameworks to enhance the electrochemical properties of PANI and other electroactive materials.

## Acknowledgements

The authors are grateful for the financial support from the National Natural Science Foundation of China (51125011, 51433001).

## Notes and references

1 J. Yan, Q. Wang, T. Wei and Z. J. Fan, *Adv. Energy Mater.*, 2014, **4**, 1300816.
2 M. D. Stoller, S. J. Park, Y. W. Zhu, J. H. An and R. S. Ruoff, *Nano Lett.*, 2008, **8**, 3498–3502.
3 Y. G. Wang and Y. Y. Xia, *Adv. Mater.*, 2013, **25**, 5336–5342.
4 Y. P. Zhai, Y. Q. Dou, D. Zhao, P. F. Fulvio, R. T. Mayes and S. Dai, *Adv. Mater.*, 2011, **23**, 4828–4850.
5 H. Jiang, P. S. Lee and C. Z. Li, *Energy Environ. Sci.*, 2012, **6**, 41–53.
6 Y. Huang, J. J. Liang and Y. S. Chen, *Small*, 2012, **8**, 1805–1834.
7 K. Wang, H. P. Wu, Y. N. Meng and Z. X. Wei, *Small*, 2014, **10**, 14–31.
8 G. A. Snook, P. Kao and A. S. Best, *J. Power Sources*, 2011, **196**, 1–12.
9 K. Zhang, L. L. Zhang, X. S. Zhao and J. S. Wu, *Chem. Mater.*, 2010, **22**, 1392–1401.
10 J. J. Xu, K. Wang, S. Zu, B. Han and Z. X. Wei, *ACS Nano*, 2010, **4**, 5019–5026.
11 Q. Wu, Y. X. Xu, Z. Y. Yao, A. R. Liu and G. Q. Shi, *ACS Nano*, 2010, **4**, 1963–1970.
12 D. W. Wang, F. Li, J. P. Zhao, W. C. Ren, Z. G. Chen, J. Tan, Z. S. Wu, I. Gentle, G. Q. Lu and H. M. Cheng, *ACS Nano*, 2009, **3**, 1745–1752.
13 H. Zengin, W. Zhou, J. Jin, R. Czerw, D. W. Smith, L. Echegoyen, D. L. Carroll, S. H. Foulger and J. Ballato, *Adv. Mater.*, 2002, **14**, 1480–1483.
14 Z. Wei, M. Wan, T. Lin and L. Dai, *Adv. Mater.*, 2003, **15**, 136–139.
15 Y. G. Wang, H. Q. Li and Y. Y. Xia, *Adv. Mater.*, 2006, **18**, 2619–2623.
16 L. Z. Fan, Y. S. Hu, J. Maier, P. Adelhelm, B. Smarsly and M. Antonietti, *Adv. Funct. Mater.*, 2007, **17**, 3083–3087.
17 M. Dirican, M. Yanilmaz and X. W. Zhang, *RSC Adv.*, 2014, **4**, 59427–59435.
18 W. Fan, C. Zhang, W. W. Tjiu, K. P. Pramoda, C. B. He and T. X. Liu, *ACS Appl. Mater. Interfaces*, 2013, **5**, 3382–3391.
19 X. Feng, R. Li, Y. Ma, R. Chen, N. Shi, Q. Fan and W. Huang, *Adv. Funct. Mater.*, 2011, **21**, 2989–2996.
20 J. Li, H. Q. Xie, Y. Li, J. Liu and Z. X. Li, *J. Power Sources*, 2011, **196**, 10775–10781.
21 Q. Q. Zhou, Y. R. Li, L. Huang, C. Li and G. Q. Shi, *J. Mater. Chem. A*, 2014, **2**, 17489–17494.
22 C. Peng, D. Hu and G. Z. Chen, *Chem. Commun.*, 2011, **47**, 4105–4107.
23 H. L. Li, J. X. Wang, Q. X. Chu, Z. Wang, F. B. Zhang and S. C. Wang, *J. Power Sources*, 2009, **190**, 578–586.
24 Y. F. Wang, X. W. Yang, L. Qiu and D. Li, *Energy Environ. Sci.*, 2013, **6**, 477–481.
25 S. Han, D. Q. Wu, S. Li, F. Zhang and X. L. Feng, *Adv. Mater.*, 2014, **26**, 849–864.
26 Z. S. Wu, Y. Sun, Y. Z. Tan, S. B. Yang, X. L. Feng and K. Mullen, *J. Am. Chem. Soc.*, 2012, **134**, 19532–19535.
27 B. G. Choi, M. Yang, W. H. Hong, J. W. Choi and Y. S. Huh, *ACS Nano*, 2012, **6**, 4020–4028.
28 C. M. Chen, Q. Zhang, C. H. Huang, X. C. Zhao, B. S. Zhang, Q. Q. Kong, M. Z. Wang, Y. G. Yang, R. Cai and D. S. Su, *Chem. Commun.*, 2012, **48**, 7149–7151.
29 Z. L. Wang, D. Xu, H. G. Wang, Z. Wu and X. B. Zhang, *ACS Nano*, 2013, **7**, 2422–2430.
30 X. D. Huang, K. Qian, J. Yang, J. Zhang, L. Li, C. Z. Yu and D. Y. Zhao, *Adv. Mater.*, 2012, **24**, 4419–4423.
31 M. Kim, C. Lee and J. Jang, *Adv. Funct. Mater.*, 2014, **24**, 2489–2499.
32 H. S. Fan, N. Zhao, H. Wang, J. Xu and F. Pan, *J. Mater. Chem. A*, 2014, **2**, 12340–12347.
33 C. Zhang, W. W. Tjiu and T. X. Liu, *Polym. Chem.*, 2013, **4**, 5785–5792.
34 K. Chi, Z. Y. Zhang, J. B. Xi, Y. G. Huang, F. Xiao, S. Wang and Y. Q. Liu, *ACS Appl. Mater. Interfaces*, 2014, **6**, 16312–16319.
35 B. Yao, L. Y. Yuan, X. Xiao, J. Zhang, Y. Y. Qi, J. Zhou, J. Zhou, B. Hu and W. Chen, *Nano Energy*, 2013, **2**, 1071–1078.
36 L. L. Liu, Z. Q. Niu, L. Zhang, W. Zhou, X. D. Chen and S. S. Xie, *Adv. Mater.*, 2014, **26**, 4855–4862.
37 P. P. Yu, X. Zhao, Z. L. Huang, Y. Z. Li and Q. H. Zhang, *J. Mater. Chem. A*, 2014, **2**, 14413–14420.
38 H. P. Cong, X. C. Ren, P. Wang and S. H. Yu, *Energy Environ. Sci.*, 2013, **6**, 1185–1191.
39 Z. Chen, J. W. F. To, C. Wang, Z. D. Lu, N. Liu, A. Chortos, L. J. Pan, F. Wei, Y. Cui and Z. N. Bao, *Adv. Energy Mater.*, 2014, **4**, 1400207.
40 G. Hao, F. Hippauf, M. Oschatz, F. M. Wisser, A. Leifert, W. Nickel, N. Mohamed-Noriega, Z. Zheng and S. Kaskel, *ACS Nano*, 2014, **8**, 7138–7146.
41 J. Zhong, Z. Yang, R. Mukherjee, A. V. Thomas, K. Zhu, P. Sun, J. Lian, H. Zhu and N. Koratkar, *Nano Energy*, 2013, **2**, 1025–1030.
42 P. P. Yu, Y. Z. Li, X. Zhao, L. H. Wu and Q. H. Zhang, *Langmuir*, 2014, **30**, 5306–5313.
43 S. J. He, X. W. Hu, S. L. Chen, H. Hu, M. Hanif and H. Q. Hou, *J. Mater. Chem.*, 2012, **22**, 5114–5120.
44 W. Fan, Y. E. Miao, Y. P. Huang, W. W. Tjiu and T. X. Liu, *RSC Adv.*, 2015, **5**, 9228–9236.
45 C. Zhang, T. X. Liu and X. H. Lu, *Polymer*, 2010, **51**, 3715–3721.
46 C. Zhang, L. L. Ren, X. Y. Wang and T. X. Liu, *J. Phys. Chem. C*, 2010, **114**, 11435–11440.

 

47 W. S. Hummers and R. E. Offman, *J. Am. Chem. Soc.*, 1958, **80**, 1339.
48 D. A. Dikin, S. Stankovich, E. J. Zimney, R. D. Piner, G. H. B. Dommett, G. Evmenenko, S. T. Nguyen and R. S. Ruoff, *Nature*, 2007, **448**, 457–460.
49 C. Zhang, W. W. Tjiu, W. Fan, Z. Yang, S. Huang and T. X. Liu, *J. Mater. Chem.*, 2011, **21**, 18011.
50 Y. Wang, Y. P. Wu, Y. Huang, F. Zhang, X. Yang, Y. F. Ma and Y. S. Chen, *J. Phys. Chem. C*, 2011, **115**, 23192–23197.
51 M. K. Liu, Y. E. Miao, C. Zhang, W. W. Tjiu, Z. B. Yang, H. S. Peng and T. X. Liu, *Nanoscale*, 2013, **5**, 7312.
52 R. J. Chen, Y. G. Zhang, D. W. Wang and H. J. Dai, *J. Am. Chem. Soc.*, 2001, **123**, 3838–3839.